Chinese Journal of Electronics
vol. 33, no. 1, pp. 245–255, January 2024
https://doi.org/10.23919/cje.2023.00.002

RESEARCH ARTICLE

Real-Time 3D Ultrasound Imaging System Based on a Hybrid Reconstruction Algorithm

Yifei LYU[1], Yu SHEN[1], Mingbo ZHANG[2], and Junchen WANG[1]

1. *School of Mechanical Engineering and Automation, Beihang University, Beijing 100191, China*
2. *The First Medical Center, General Hospital of Chinese PLA, Beijing 100853, China*

Corresponding author: Junchen WANG, Email: wangjunchen@buaa.edu.cn
Manuscript Received January 2, 2023; Accepted April 4, 2023

Abstract — As a safe and convenient imaging technology in clinical routine diagnosis, ultrasound imaging can provide real-time 2D images of internal tissues and organs. To realize real-time 3D image reconstruction, pixel nearest neighbor interpolation (PNN) reconstruction algorithm and Bezier interpolation algorithm are combined into a hybrid reconstruction algorithm. On this basis, a real-time interactive 3D ultrasound imaging system is developed. Through temporal calibration and spatial calibration, the six degrees of freedom poses of 2D ultrasound images can be accurately collected. The 3D volume reconstructed by the proposed 3D reconstruction algorithm is visualized by volume rendering. A multi-thread software system allows parallel operation of data acquisition, 3D reconstruction, volume visualization and other functions. 3D imaging experiments on a 3D printing femur model, a neck phantom and the neck of human volunteers were performed for systematic evaluation. When the reconstruction voxel size was set to be (0.5^3 mm^3, 1.0^3 mm^3, 1.5^3 mm^3), the reconstruction errors of the femur and trachea model were respectively (0.23 mm, 0.31 mm, 0.56 mm) and (0.62 mm, 0.88 mm, 1.41 mm). Clinical feasibility was demonstrated by application of the 3D ultrasound imaging on the neck of human volunteers.

Keywords — 3D ultrasound imaging, Free-hand reconstruction, Spatial calibration.
Citation — Yifei LYU, Yu SHEN, Mingbo ZHANG, *et al.*, "Real-Time 3D Ultrasound Imaging System Based on a Hybrid Reconstruction Algorithm," *Chinese Journal of Electronics*, vol. 33, no. 1, pp. 245–255, 2024. doi: 10.23919/cje.2023.00.002.

I. Introduction

The accurate diagnosis and treatment of modern medicine needs the information support of medical imaging. With the development of intraoperative navigation system and robot technology, how to obtain real-time 3D spatial structure of patients has become an urgent problem to be solved. Computerized tomography (CT) and magnetic resonance imaging (MRI) can provide 3D images of the human body with high accuracy. With the use of C-arm CT, real-time intraoperative imaging has been achieved [1]. However, these imaging techniques have some problems, such as radiation, large equipment and high cost. Ultrasound (US) imaging does not have the above problems and has better real-time and soft tissue imaging effect. Nowadays, 2D US imaging is more widely used than 3D US imaging because of its higher image quality and lower cost. At the same time, the reading of 2D US images has a higher requirement on the knowledge and experience of doctors. There is a higher demand for 3D US imaging in the examination of fetuses, spines and other organs [2]–[4].

3D US imaging techniques can be divided into two main categories depending on the transducer used. One is using a 2D matrix transducer [5] or a spherically curved array transducer [6] to generate 3D US images directly. However, the process of making a 2D matrix transducer or a spherically curved array transducer is complicated and expensive, and the resolution of the generated image is low. Another one is still using the traditional transducer. 3D images are reconstructed by collecting six degrees of freedom (6-DoF) poses of 2D US images. Compared with the first category, the 3D images produced by such methods are of higher quality and the operation is more flexible. The process of 3D US imaging using 2D US images with known 6-DoF poses can be divided into three steps: data acquisition, 3D re-

Associate Editor: Prof. Mingyue DING, Huazhong University of Science and Technology.

construction and volume visualization.

The key of the data acquisition stage is to accurately obtain the 6-DoF pose of each 2D US image. The existing 6-DoF pose acquisition methods can be divided into sensorless and sensor-based. Sensorless methods use algorithms, such as speckle decorrelation [7] and machine learning [8], to predict the relative pose relationship of adjacent 2D US images. In this way, 3D images can be obtained without any additional equipment. However, there is a large cumulative error. Even if the addition of small sensors, such as inertial measurement unit (IMU) [9], can reduce the error while retaining the original advantages, it is still difficult to use for large-scale imaging. In the sensor-based approach, a sensor or a device, such as optical measurement systems [10], electromagnetic measurement systems [11], [12], vision systems [13], robots [14]–[16] and mechanical devices [17], [18], is installed on the US probe to capture its 6-DoF pose. Chan *et al.* even tried to implement pose collection using a game controller [19]. The sensor-based methods have higher accuracy than the sensorless methods, but the operation is limited by the existence of sensors. Many studies have reduced this limitation through equipment improvement [20] and algorithm design [21].

3D reconstruction is to convert 2D images with known 6-DoF poses into a structured 3D volume with reconstruction algorithm. Point cloud data is the easiest to generate, but only for small amounts of data [13]. In order to facilitate subsequent visualization and data processing, 3D data is usually set in 3D voxel grid form. The existing reconstruction algorithms in 3D voxel grid form can be divided into three categories: pixel-based methods (PBMs), voxel-based methods (VBMs) and function-based methods (FBMs). PBMs traverse each pixel of each 2D image to update the voxel values in its neighborhood, such as pixel nearest neighbor interpolation (PNN) [22], [23], pixel trilinear interpolation (PTL) [23] and squared distance weighted interpolation (SDW) [24]. So PBMs are often used in real-time 3D imaging systems [12], [23]. VBMs traverses each voxel in the grid and calculates its value based on the values of pixels in its neighborhood, such as voxel nearest neighbor (VNN) [25] and distance weighted (DW) [26]. VBMs can complete 3D reconstruction quickly when all data collection is completed. FBMs use the function, such as radial basis function (RBF) [27] and Bezier curve [28], fitted by values and coordinates of pixels to calculate values of voxels. Even with a small amount of data, FBMs can ensure the continuity of reconstruction results.

Due to the limitation of technology, the existing 3D ultrasound imaging system is difficult to meet the requirements of clinical application. Chen *et al.* used a wireless real-time 3D US imaging system to image the human spine, but the imaging accuracy was low [29]. Jiang *et al.* also achieved rapid reconstruction of a complete human spine [30]. However, limited by the visualization method, it can only be used for scoliosis assessment. Xing *et al.* designed a 2D/3D US/CT-guided system for percutaneous focal liver thermal ablation, but the accuracy still needs to be further verified [31].

In order to meet the needs of clinical application, we propose a real-time interactive 3D US imaging system. During the scanning process, the system can simultaneously reconstruct and display high quality 3D images. Interactive functions can meet a variety of clinical needs. An improved spatial calibration method [32] is used to calibrate the US probe. The 3D voxel grid is updated by a hybrid reconstruction algorithm combining Bezier interpolation [28] and PNN algorithm [23]. The reconstructed 3D volume is visualized by ray-casting rendering on the GPU. A multi-thread software system is proposed to implement the above functions in parallel. The clinical feasibility of the system has been verified by various experiments on models and human.

The research was presented at the 2022 World Robot Conference Symposium on Advanced Robotics and Automation (2022 WRC SARA) [33]. In this paper, the calibration methods and results, experimental methods and results as well as the improved reconstruction error calculation method will be introduced in more detail.

II. Methods

1. System description

The components of the real-time interactive 3D US imaging system are shown in Figure 1.

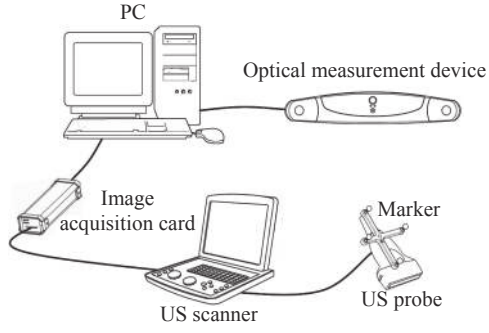

Figure 1 The components of the real-time 3D US imaging system.

The system consists of three main parts: US image acquisition system, pose acquisition system and computer system. US image acquisition system contains a portable US scanner (M9T, Mindray Corporation, Shenzhen, China) with a linear 2D US probe (L12-4S). 2D US images are transmitted from the US image acquisition system to the computer system with using an image acquisition card (TC-UB 530, TCHD, Beijing, China). Pose acquisition system is used to obtain 6-DoF poses of the US probe. It contains an optical measurement device (Polaris Vega, NDI, Ontario, Canada) and an optical marker mounted on the US probe. Computer system contains a PC (AMD Ryzen 7 5800 H with Radeon Graphics 3.20 GHz, 16 GB RAM and Nvidia GeForce RTX 3050Ti)

and a multi-thread software system programmed with C++. The software system uses the collected data for 3D reconstruction and realizes 3D image visualization and user interaction through a graphical interface.

2. Temporal calibration

Because the collected data does not contain a time stamp and there is an unknown time difference in the data transmission process, the time axes of image data and pose data are not aligned. Therefore, it is necessary to obtain the unknown time difference between the two types of data by temporal calibration. Rousseau *et al.* proposed a calibration method [34]. We simplified it so that the temporal calibration could be done quickly. The US probe moves up and down quasi-periodically in a sink filled with water. During this time, the bottom of the sink should always be within US imaging range. At the same time, US images and 6-DoF poses are collected from the US scanner and optical measurement equipment. The bottom of the sink is extracted from the US image by the linear detection algorithm. The vertical displacement curves with time are calculated by using two kinds of data collected respectively. Then the time differences between the two curves at the highest positions and the lowest positions are calculated. The average is considered to be the time difference between the two kinds of data.

3. Spatial calibration

3D reconstruction requires 2D images with known 6-DoF poses. However, the data provided by the optical measuring device is the 6-DoF pose of the marker installed on the US probe, rather than the 2D US image. We improve a US probe spatial calibration method designed by Wen *et al.* [32] to calculate the relative pose relationship between the 2D US image and the marker. This method has high precision, simple operation and low cost.

For spatial calibration, a stylus (standard Polaris stylus, NDI, Ontario, Canada) was adjusted so that its tip was just on the 2D US image plane. As shown in Figure 2, let $\{I\}$ represent the 2D US image coordinate system, $\{M\}$ represent the marker coordinate system, $\{W\}$ represent the optical measurement device coordinate system and $\{S\}$ represent the stylus coordinate system. The coordinate of the stylus tip in the marker coordinate system can be described as

$$^{M}\boldsymbol{P} = {}^{W}_{M}\boldsymbol{T}^{-1}\,{}^{W}_{S}\boldsymbol{T}\,{}^{S}\boldsymbol{P} \tag{1}$$

where $^{M}\boldsymbol{P}$ is the coordinates of the stylus tip in the marker coordinate system and $^{S}\boldsymbol{P}$ is the coordinates of the stylus tip in the stylus coordinate system. ${}^{W}_{M}\boldsymbol{T}$ and ${}^{W}_{S}\boldsymbol{T}$ are the corresponding homogeneous transformation matrices. The coordinates of the pixel in the stylus coordinate system is caculated by a pointer calibration [35].

The tip of the stylus appears as a bright white point on the US image. The coordinate of the tip in the 2D US image can be obtained by manual selection.

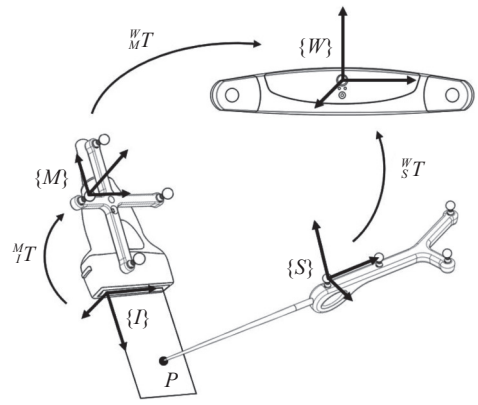

Figure 2 Schematic diagram of spatial calibration.

$$^{I}\boldsymbol{P} = [s_x u, s_y v, 0, 1]^{\mathrm{T}} \tag{2}$$

where $^{I}\boldsymbol{P}$ is the coordinate of the stylus tip in the 2D US image and (u, v) is the 2D pixel coordinate of the stylus tip in the 2D US image. s_x and s_y are the scaling factors representing the pixel spatial resolution along the x and y direction.

Multiple sets of coordinates can be obtained by changing the position of the stylus tip on the US image. The relative pose relationship between the 2D US image and the marker was obtained by registering two groups of point clouds in 2D US image coordinate system and marker coordinate system by singular value decomposition (SVD) method [36].

For ease of operation, the spatial calibration is performed using the device shown in Figure 3.

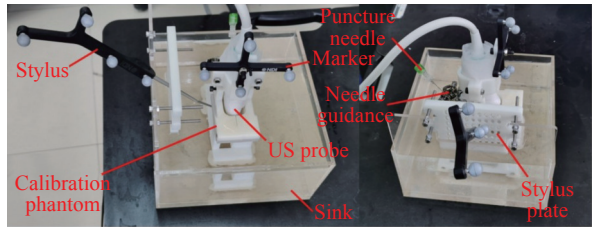

Figure 3 The device of spatial calibration.

A calibration phantom fixed in a water sink is used for fixing the US probe. A stylus plate is set on the side of the sink. Four adjusting bolts between the stylus plate and the sink are used to fine-tune the position of stylus so that the stylus tip is in the US image plane. The position of the stylus tip on the US image can be changed by placing the stylus in different holes on the stylus plate. A needle guidance keeping a puncture needle indicates the physical spatial position of the 2D US image. Just make sure the stylus tip is in contact with the puncture needle.

In order to verify the accuracy of the spatial calibration, nine additional sets of data were collected to calculate the error. The formula of root-mean-square error (RMSE) is expressed as follows.

$$\mathrm{RMSE}=\sqrt{\frac{1}{N}\sum\left\|{}_{I}^{M}\boldsymbol{T}^{I}\boldsymbol{P}_i-{}^{M}\boldsymbol{P}_i\right\|} \tag{3}$$

where $\|\cdot\|$ is the Euclidean norm. ${}_{I}^{M}\boldsymbol{T}$ is the homogeneous transformation matrix computed by spatial calibration. N is the number of data groups.

4. Hybrid reconstruction algorithm

In the 3D US imagine system, a volume in the form of a 3D voxel grid is predefined for 3D reconstruction. As shown in Figure 4, let $\{V\}$ represent the volume coordinate system. The coordinate transformation from pixels of 2D images to volume voxels can be described as

$$^{V}\boldsymbol{P}={}_{W}^{V}\boldsymbol{T}{}_{M}^{W}\boldsymbol{T}{}_{I}^{M}\boldsymbol{T}^{I}\boldsymbol{P} \tag{4}$$

where $^{V}\boldsymbol{P}$ is the coordinates in the volume coordinate system and $^{I}\boldsymbol{P}$ is the coordinates in the 2D US image coordinate system. ${}_{W}^{V}\boldsymbol{T}$, ${}_{M}^{W}\boldsymbol{T}$, ${}_{I}^{M}\boldsymbol{T}$ are the corresponding homogeneous transformation matrices.

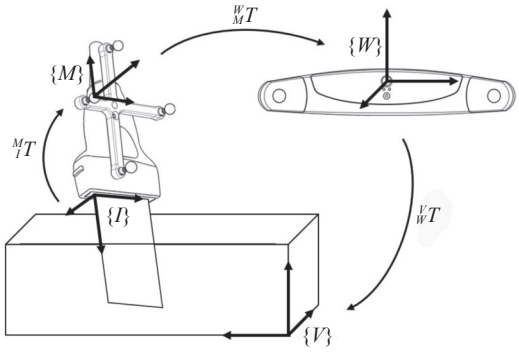

Figure 4 The transformation relationships among the 2D US image, the marker, the optical measurement device and the volume.

After coordinate transformation, the voxel values need to be calculated by reconstruction algorithm. Nowadays, few reconstruction algorithms can meet both real-time performance and high precision [37]. The PNN algorithm [38] is widely used in incremental reconstruction because of its small computation and its ability to calculate a single image. However, it is difficult to guarantee the continuity and smoothness of reconstruction results. Huang *et al.* realized fast reconstruction of sparse data by using Beizer interpolation [28]. Compared with other algorithms, this algorithm takes into account the reconstruction speed and the continuity of the reconstruction result. However, the low accuracy and the inability to repeat the scan make it less useful. In this paper, a hybrid algorithm combining PNN reconstruction algorithm and Bezier interpolation algorithm is used to achieve real-time reconstruction with high precision, repeatable scanning and good continuity.

As shown in Figure 5, each reconstruction uses four 2D images with known 6-DoF poses to fit a Bezier curve to determine voxels to be updated and their values. In order to ensure continuity and smoothness, there will be two identical 2D images in two adjacent reconstructions. Pixels in the same position on the four images are used as control points to fit a cubic Bezier curve.

$$\begin{aligned}\boldsymbol{P}(t)=&\boldsymbol{P}_1(1-t)^3+3\boldsymbol{P}_2t(1-t)^2\\&+3\boldsymbol{P}_3t^2(1-t)+\boldsymbol{P}_4t^3,\quad t\in[0,1]\end{aligned} \tag{5}$$

where $\boldsymbol{P}(t)$ is 3D coordinates and value of the point on the Bezier curve, t is the normalized parameter of the position on the Bezier curve and $\boldsymbol{P}_1$, $\boldsymbol{P}_2$, $\boldsymbol{P}_3$, $\boldsymbol{P}_4$ are the control points. A control point $\boldsymbol{P}$ can be described as

$$\boldsymbol{P}=[p_x,p_y,p_z,p_v]^{\mathrm{T}} \tag{6}$$

where (p_x,p_y,p_z) is the 3D coordinates of $\boldsymbol{P}$ in the volume coordinate system, and p_v is the value of $\boldsymbol{P}$.

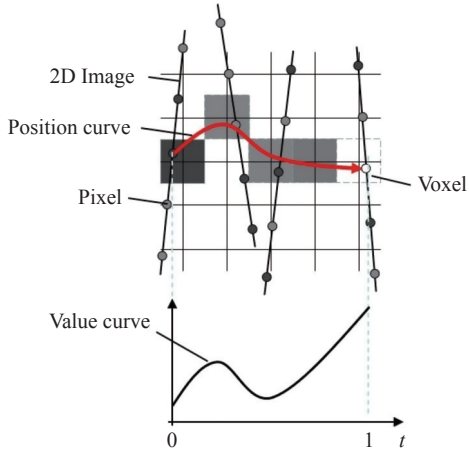

Figure 5 Bezier curve fitted with four 2D images.

The values calculated from the Bezier curves are not directly assigned to the voxels. The weighted average assignment method in PNN algorithm is used to update the voxel value. The predefined volume contains two 3D voxel grids, V and W. Values of voxels are recorded in V, and weight values of voxels are recorded in W. Before each reconstruction, assume that the value of the voxel of coordinates (i,j,k) is $V(i,j,k)_n$ and its weight is $W(i,j,k)_n$. The value calculated using Bezier curve is v and the weight is w (default is 1). The values of V and W at the coordinates (i,j,k) are updated to

$$V(i,j,k)_{n+1}=\frac{V(i,j,k)_nW(i,j,k)_n+vw}{W(i,j,k)_n+w} \tag{7}$$

$$W(i,j,k)_{n+1}=W(i,j,k)_n+w \tag{8}$$

where $V(i,j,k)_{n+1}$ and $W(i,j,k)_{n+1}$ are the new value and new weight value of voxel at coordinates (i,j,k), respectively.

Due to the limitation of computing performance, the 2D images need to be down-sampled to speed up the computational speed of reconstruction. Downsampling reduces the number of pixels involved in computation, thus realizing real-time reconstruction. In order to ensure the

accuracy of reconstruction results, the down-sampling coefficient should not be too large. In this study, the down-sampling coefficient is 2.

By the method shown in Algorithm 1, each time a 2D US image and its pose are collected, 3D reconstruction can be performed once. The hybrid reconstruction algorithm not only satisfies the real-time and high precision, but also ensures the continuity and smoothness of the results.

Algorithm 1 Hybrid reconstruction algorithm

Predefine: V: 3D voxel grids for voxel values; W: 3D voxel grids for weight values; DataQueue: queue for 2D images and their 6-DoF poses.

Input: Image: 2D image; *Pose* 6-DoF pose of 2D image.

```
Image = downsample(Image);
Put (Image, Pose) into DataQueue;
if (size of DataQueue ≥ 4)
 Take out the first two in the DataQueue;
 Copy the first two in the DataQueue;
 Repeat until (traverse all pixel positions of 2D image)
   Compute four control points;
   Compute Bezier curve;
   Repeat until (traverse all voxels on the Bezier curve)
     Update V and W.
```

5. 3D visualization

With using the ray casting method based on a GPU, real-time volume rendering is realized by the visualization toolkits (VTK, KitwareInc, New York, USA). Interactive tools are designed to allow users to freely adjust the color and transparency of 3D images. To make it easier for doctors to operate during scans and surgeries, the US probe is also visualized on 3D image with using the VTK.

6. Multi-thread software system

The software system requires data acquisition, 3D reconstruction and visualization in real-time. As shown in Figure 6, the software system consists of eight threads to perform multiple tasks simultaneously.

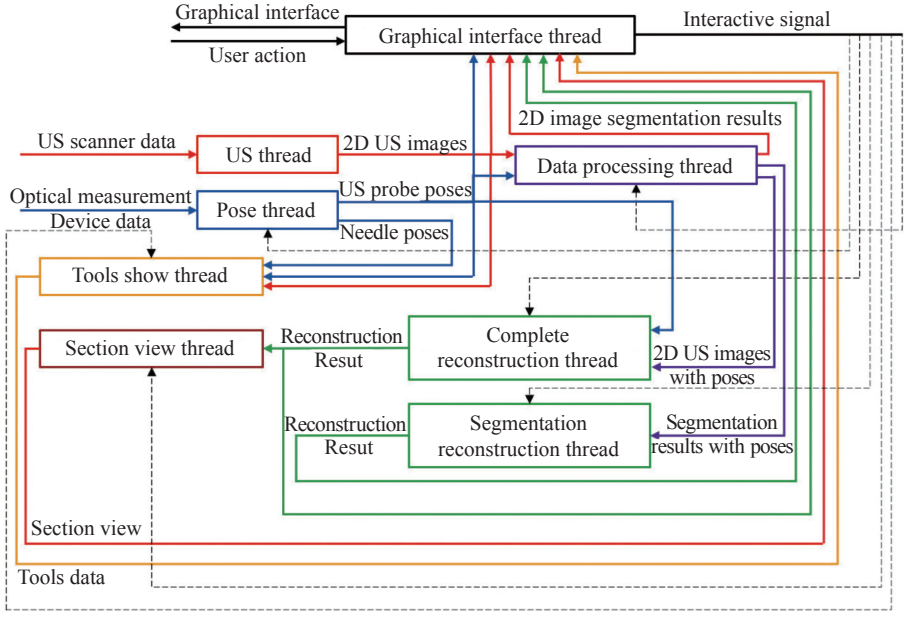

Figure 6 The structure of multi-thread software system.

The next steps describe the functionality of each thread and the transfer of data between them.

- Graphical interface thread: The graphical interface will run in this thread. Receive data from other threads, such as 2D images, 3D images, 6-DoF poses and segmentation results, and display them on the interface. After the user uses the interactive tools on the interface, this thread will send interactive signals to other threads. Rendering with VTK is also done in this thread.
- US thread: Receive 2D US images from the US scanner and send them to other threads at 30 frames per second.
- Pose thread: Receive 6-Dof poses of the marker from the optical measurement device and send them to other threads at 30 frames per second.
- Data processing thread: In this thread, 2D US images are segmented using an algorithm chosen by the user. 2D images and 6-DoF poses are matched one by one with using the result of the temporal calibration. 2D images with known 6-DoF poses are sent to other threads.
- Complete reconstruction thread: The volume is updated by the hybrid reconstruction algorithm with using 2D US images with known 6-DoF poses. What's more, the volume is predefined and segmented in this thread. The volume is sent to other threads.
- Segmentation reconstruction thread: The volume is updated by the hybrid reconstruction algorithm using 2D image segmentation results with known 6-DoF poses.

The volume is sent to other threads.

• Tools show thread: In this thread, 3D images with known 6-DoF poses of tools, such as the US probe and puncture needle, are generated. Then the data is sent to Graphical Interface Thread to implement tools visualization.

• Section view thread: Receive the volume sent by the Complete Reconstruction Thread. The sectional view is generated using the 6-DoF pose of the section plane selected by the user and sent to the Graphical Interface Thread for visualization.

7. 3D imaging experiments on phantoms

In order to verify the feasibility of the proposed system and test the accuracy, 3D imaging experiments on a femur model and a neck phantom were carried out.

The femur model was 3D printed using resin material. Since the femur model was placed in the water during the scanning process, the accuracy of the freehand scanning will be reduced because of hand shaking due to lack of support. As shown in Figure 7, the US probe is mounted on a KUKA iiwa7 robot arm to scan the femur model to rule out the effects of hand shaking. The robot arm will follow a predefined trajectory to scan the entire end of the femur model. The surface of the femur model is segmented with using a threshold segmentation algorithm.

The neck phantom is a resinous solid cube containing a trachea, an esophagus, blood vessels, thyroid gland and two thyroid nodules. After the scan was complete, the color and transparency were changed through the interactive tool of the software system. The purpose is to clearly distinguish the various tissues and organs from the 3D image.

In order to evaluate the accuracy of the 3D US imaging system, the reconstruction errors in experiments were calculated. The 3D printed femur model had the original 3D data. The accurate 3D data of the trachea model in the neck phantom was obtained by CT scanning. The accurate 3D data of phantoms are compared with the imaging results of the 3D US system to calculate reconstruction errors.

The reconstruction error was calculated using the Medical Image Computing System software (MICSys, https://mrs.buaa.edu.cn/?page_id=342) developed by our laboratory. The voxels representing the surface of the femur model or trachea were segmented from the reconstructed volume through threshold segmentation and connected domain selection. With using morphological closing operation, the defects caused by segmentation were repaired. The outer surface of the segmented voxels was extracted and smoothed. Since US imaging of the surface of the femur model or tracheal has a certain thickness, the extracted surface data were double layers. Only the outer surface was retained by manual selection. The extracted surface data were registered with accurate 3D data. The RMSE of the registration was taken as the reconstruction error.

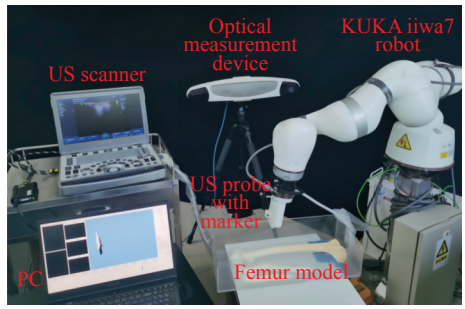

Figure 7 The experiment scene of femur model 3D imaging.

8. 3D imaging experiments on human volunteers

The 3D imaging experiments on human volunteers were performed to verify the clinical feasibility of our system. A sonographer with years of clinical experience performed an ultrasound scan on the neck of 3 human volunteers. Two of them had thyroid nodules no larger than 3 mm in diameter. Four physicians evaluated the quality of the 3D images generated in real time by examining the imaging of carotid arteries, thyroid gland and thyroid nodules.

In order to verify the feasibility of the 3D US imaging system for real-time segmentation of tissue and organ, an additional scan of the carotid artery was performed. A circle detection algorithm based on Hough transform is used to segment the carotid artery. During the scan, a complete 3D US image and a separate 3D image of the carotid artery were generated simultaneously.

In all experiments, the depth of the US imaging was set to be 5 cm. The resolution of 2D US images was 600×800 and the pixel size was 0.063 mm $\times$ 0.063 mm. The frame rates of 2D US image acquisition and 6-DoF pose acquisition were both 30 frames per second (FPS). The down-sampling coefficient was set to be 4.

III. Results

1. Temporal calibration

The variation curves of vertical displacement with time directly drawn using the data collected from the US scanner and the optical measurement device are shown in Figure 8(a). Apart from the beginning and the end, each curve contains three highest points and four lowest points. The average of the time difference between the highest or lowest point corresponding to the two curves is taken as the unknown time difference between the two kinds of data. The variation curves of vertical displacement with time after eliminating time difference is shown in Figure 8(b).

The two curves basically coincide after temporal calibration. Due to the hand-held US probe in the calibration process, the US image cannot be guaranteed to be strictly vertical. Therefore, the two curves don't exactly coincide, like the beginning and the end. Due to the automatic algorithm, the bottom position of the sink in

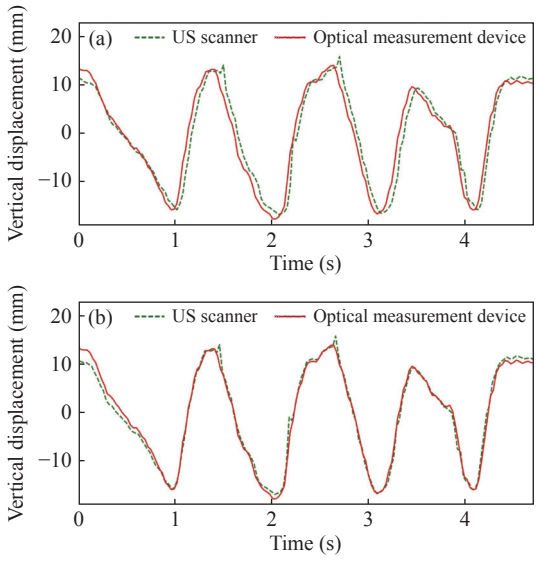

Figure 8 The variation curves of vertical displacement with time. (a) Original data; (b) After eliminating time difference.

some images has not been accurately extracted. Therefore, there are mutation points in the curve representing the image data, such as the first and second-highest points. These mutation points were eliminated in the calculation process.

2. Spatial calibration

The spatial calibration was carried out for 5 times. In each calibration, 9 sets of data are used to calculate ${}^{M}_{I}\boldsymbol{T}$, and the other 9 sets of data are used to calculate calibration error. The calibration errors are shown in Table 1, where FRE is the RMSE of registration in the calibration and TRE is the calibration error calculated using equation (3).

Table 1 Spatial calibration errors

	1	2	3	4	5
FRE (mm)	0.4557	0.4462	0.5159	0.6573	0.6168
TRE (mm)	0.8978	0.9531	0.7003	0.7391	0.9750

The calibration errors were all less than 1 mm. Due to the low FRE value and the lowest TRE value, the result of the third spatial calibration was used for the subsequent 3D reconstruction experiments.

3. 3D imaging experiments on phantoms

The processes of 3D imaging experiments on the femur model and the neck phantom were carried out as shown in Figure 9(a) and (b). The sizes of the reconstructed volumes are shown in Table 2. The scanning process of the femur model shows 3D images with threshold segmentation. The scanning processes of the neck phantom shows original 3D images.

The 3D imaging result of the femur model is shown in Figure 10(a). In order to make the original 3D data of the neck phantom more intuitive, interactive tools were used to adjust them. As shown in Figure 10(b), the adjusted 3D image of the neck phantom can clearly present various tissues and organs, such as the trachea, the thyroid gland, blood vessels and thyroid nodules.

The 3D imaging experiments of the femur model and the neck phantom were repeated five times with the voxel size of 0.5^3 mm^3, 1.0^3 mm^3 and 1.5^3 mm^3, respectively. The surface of the femur model or trachea model extracted from the reconstructed volume was registered with the original 3D data or CT scan data. The registration results are shown in Figure 11. The mean and standard deviation (SD) of the reconstruction errors for different voxel sizes are shown in Table 3.

The real-time 3D US imaging system has high reconstruction accuracy. With the increase of the voxel size, the reconstruction results are smoother. However, reconstruction errors increase and some details are missing due to the reduced resolution. The reconstruction errors and SD of the femur model are smaller than those of the trachea model. This shows that robot scanning has higher imaging accuracy and stability than freehand scanning.

4. 3D imaging experiments on human volunteers

The processes of 3D imaging experiments on human volunteers were carried out as shown in Figure 9(c) and (d). The sizes of the reconstructed volumes are shown in Table 2. During the scanning progress of the human carotid artery, the black part is original 3D images and the red part is 3D images of the segmented carotid artery. According to the graphical interface display results, the real-time 3D US imaging system can follow the US probe to achieve real-time incremental reconstruction. The reconstruction results have excellent continuity and smoothness. Moreover, repeated scanning of the same area does not adversely affect the imaging results.

Due to the influence of the surrounding tissue, it was difficult to separate 3D images of the human by adjusting the color and transparency. Although the circle detection algorithm can segment the carotid artery, the continuity and smoothness of the segmentation results still have room of improvement.

The involved clinical practitioners can clearly distinguish the tissues and organs from the 3D image of the neck phantom. For human volunteer imaging, as shown in Figure 10(c), tissues and organs can be clearly observed after manual segmentation. The involved clinical practitioners had positive comments on the feasibility of the system for clinical application.

IV. Discussion

In this paper, a real-time interactive 3D US imaging system is implemented. Through temporal calibration and spatial calibration, the 6-DoF poses of 2D US images are accurately obtained. A hybrid reconstruction algorithm, combining Bezier interpolation and PNN reconstruction, achieves both real-time and continuous reconstruction. Compared with the Bezier interpolation algorithm [28], our algorithm can not only realize the re-

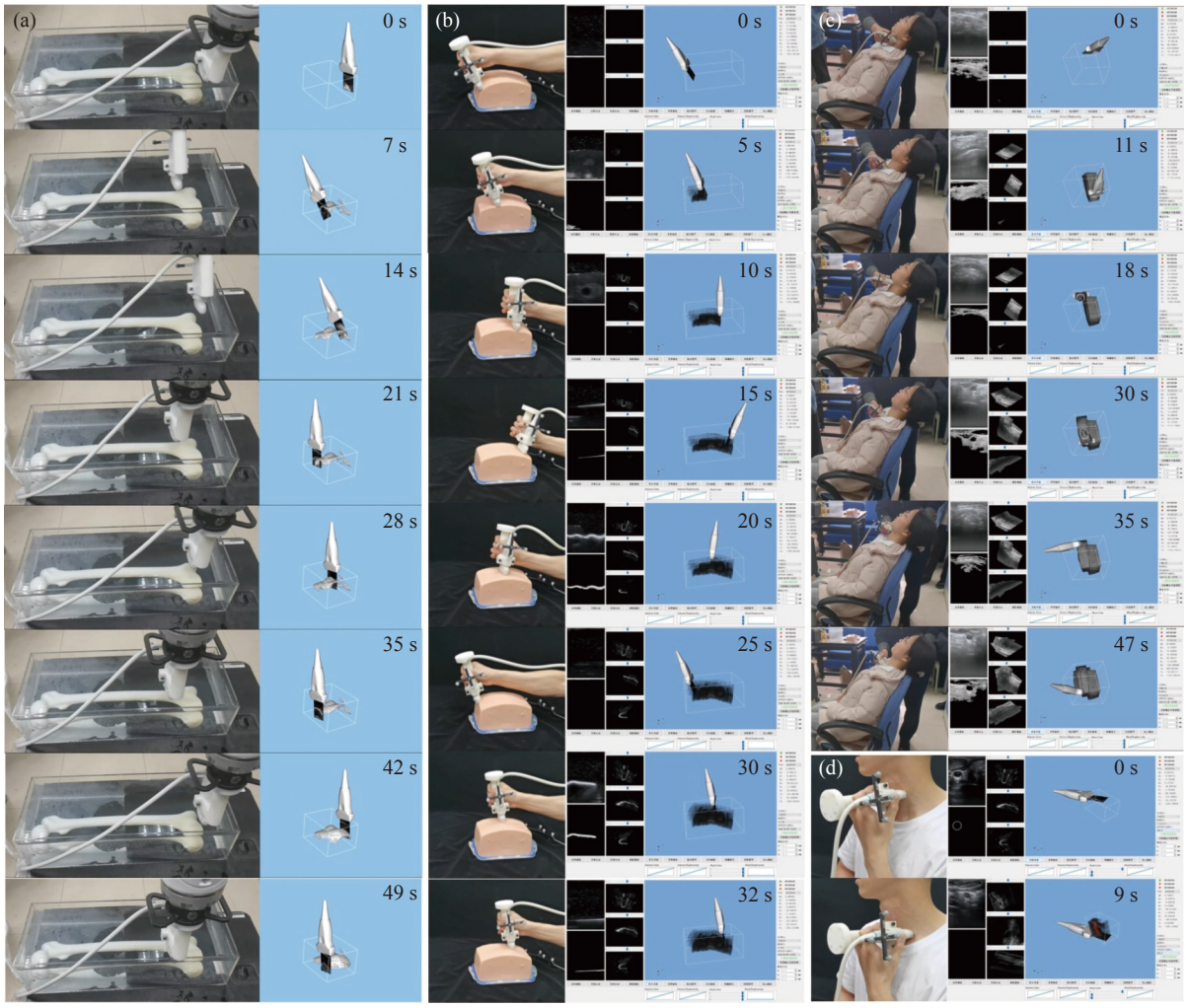

Figure 9 The process of 3D imaging experiments. (a) Femur model; (b) Neck phantom; (c) Human; (d) Human carotid artery.

Table 2 The sizes of the reconstructed volumes

	Size of reconstructed volume
Femur model	76 mm × 84 mm × 106 mm
Neck phantom	68 mm × 175 mm × 121 mm
Human 1	65 mm × 67 mm × 108 mm
Human 2	82 mm × 94 mm × 112 mm
Human 3	79 mm × 83 mm × 107.5 mm
Carotid artery	46 mm × 83 mm × 55 mm

construction of sparse data, but also improve the image quality by repeated scanning in the same position.

In the experiment, the real-time 3D US imaging of the models and human tissues is successfully realized using our system. The 3D imaging on human body is more complex, and the muscle tissue joined together is difficult to remove. Organs that are more responsive to ultrasound, like bones, are more easily to be segmented with using segmentation algorithms. Further research may focus on changing or adding advanced 2D or 3D image segmentation algorithms to improve the 3D image quality.

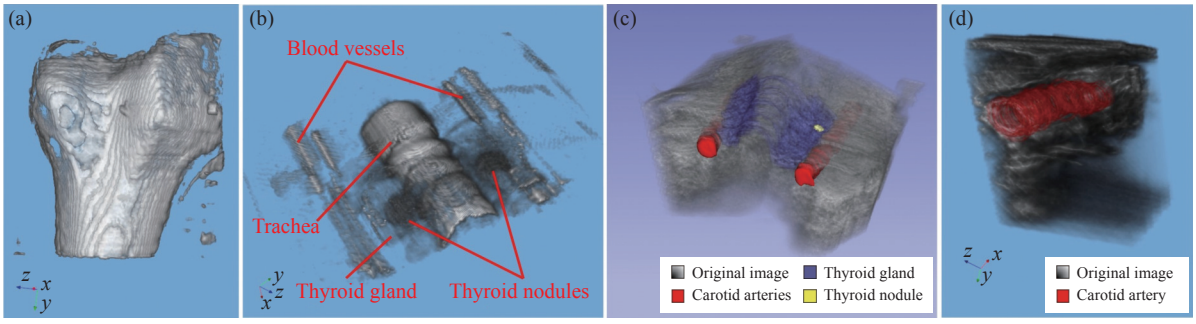

Figure 10 3D imaging results. (a) Femur model; (b) Neck phantom; (c) Human; (d) Carotid artery of human.

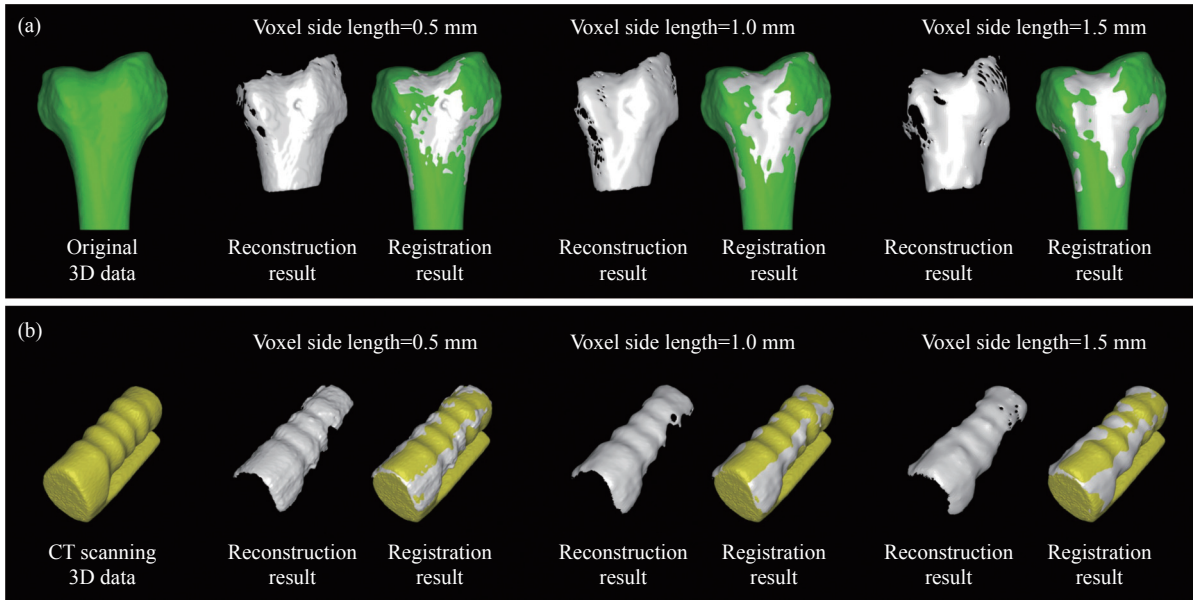

Figure 11 Registration results. (a) Femur model; (b) Trachea model.

Table 3 Reconstruction errors

Voxel size	Femur model		Trachea model	
	Mean (mm)	SD (mm)	Mean (mm)	SD (mm)
0.5^3 mm3	0.2284	0.0046	0.6164	0.0667
1.0^3 mm3	0.3145	0.0120	0.8841	0.0494
1.5^3 mm3	0.5551	0.0248	1.4108	0.2088

In addition to excellent real-time and interactive functions, the system also has excellent reconstruction accuracy. Most of the calculated reconstruction errors are even smaller than the length of the voxel sides. This is also due to the surface extraction operation of the reconstruction results in the error calculation process.

With the increase of the voxel size, the increase of reconstruction error and SD is easy to understand. However, the experimental results showed that the SD of trachea model with the voxel size of 1.0 mm was smaller than that with the voxel size of 0.5 mm. After analysis, when the voxel size is small, the main source of the instability of reconstruction is the handshake. The reduction of resolution reduces the effect of handshake on imaging results. The larger reconstruction error of the tracheal model compared with the femur model is also due to the instability of freehand scanning.

Although the clinical feasibility of our system has been verified through experiments, there is still a long way to march before the actual clinical application. The current system requires the patient to remain still in the duration of the scan, otherwise the results will be misaligned and deformed. In addition, the patient's breathing will also affect the imaging accuracy. There are studies using the visual system to track the patient's move [39]. In the follow-up work, we will also try to add the patient tracking function into the system.

V. Conclusion

We have proposed a real-time interactive 3D US imaging system using a hybrid reconstruction algorithm combining Bezier interpolation and PNN reconstruction. The system can present 3D images while scanning. Imaging results have high accuracy, good continuity, good smoothness and can be improved by repeated scanning. Interactive functions meet the clinical needs of clinical practitioners. The experimental results confirmed the feasibility of the system in clinical application.

Acknowledgement

This work was supported by the National Key R&D Program of China (Grant No. 2022YFC2405401) and the National Natural Science Foundation of China (Grant No. 62173014).

References

[1] S. Waldeck, S. Schmidt, C. von Falck, *et al.*, "New hybrid multiplanar cone beam computed tomography-laser-fluoroscopic-guided approach in cochlear implant surgery," *International Journal of Computer Assisted Radiology and Surgery*, vol. 17, no. 10, pp. 1837–1843, 2022.

[2] A. L. Zimerman, "The use of two-dimensional (2D), three-dimensional (3D) ultrasound and fetal Doppler studies in the first stage of labor," in *Intrapartum Ultrasonography for Labor Management*, A. Malvasi, Ed. Springer, Cham, pp. 133–143, 2021.

[3] T. T. Y. Lee, K. K. L. Lai, J. C. Y. Cheng, *et al.*, "3D ultrasound imaging provides reliable angle measurement with validity comparable to X-ray in patients with adolescent idiopathic scoliosis," *Journal of Orthopaedic Translation*, vol. 29, pp. 51–59, 2021.

[4] F. Cenni, S. H. Schless, L. Bar-On, *et al.*, "Reliability of a clinical 3D freehand ultrasound technique: analyses on healthy and pathological muscles," *Computer Methods and Programs in Biomedicine*, vol. 156, pp. 97–103, 2018.

[5] M. Mozaffarzadeh, M. Soozande, F. Fool, *et al.*, "Receive/transmit aperture selection for 3D ultrasound imag-

ing with a 2D matrix transducer," *Applied Sciences*, vol. 10, no. 15, article no. 5300, 2020.

[6] E. Hayashi, N. Kanno, R. Shintate, *et al.*, "3D ultrasound imaging by synthetic transmit aperture beamforming using a spherically curved array transducer," *Japanese Journal of Applied Physics*, vol. 61, no. SG, article no. SG1034, 2022.

[7] R. J. Housden, A. H. Gee, G. M. Treece, *et al.*, "Sensorless reconstruction of unconstrained freehand 3D ultrasound data," *Ultrasound in Medicine & Biology*, vol. 33, no. 3, pp. 408–419, 2007.

[8] H. T. Guo, S. Xu, B. Wood, *et al.*, "Sensorless freehand 3D ultrasound reconstruction via deep contextual learning," in *Proceedings of the 23rd International Conference on Medical Image Computing and Computer Assisted Intervention*, Lima, Peru, pp. 463–472, 2020.

[9] R. Prevost, M. Salehi, S. Jagoda, *et al.*, "3D freehand ultrasound without external tracking using deep learning," *Medical Image Analysis*, vol. 48, pp. 187–202, 2018.

[10] H. Moon, G. Ju, S. Park, *et al.*, "3D freehand ultrasound reconstruction using a piecewise smooth Markov random field," *Computer Vision and Image Understanding*, vol. 151, pp. 101–113, 2016.

[11] M. I. Daoud, A. L. Alshalalfah, F. Awwad, *et al.*, "Freehand 3D ultrasound imaging system using electromagnetic tracking," in *Proceedings of 2015 International Conference on Open Source Software Computing*, Amman, Jordan, pp. 1–5, 2015.

[12] Z. P. Chen and Q. H. Huang, "Real-time freehand 3D ultrasound imaging," *Computer Methods in Biomechanics and Biomedical Engineering:Imaging & Visualization*, vol. 6, no. 1, pp. 74–83, 2018.

[13] J. Meza, S. H. Contreras-Ortiz, L. A. Romero, *et al.*, "Three-dimensional multimodal medical imaging system based on freehand ultrasound and structured light," *Optical Engineering*, vol. 60, no. 5, article no. 054106, 2021.

[14] Q. H. Huang, J. L. Lan, and X. L Li, "Robotic arm based automatic ultrasound scanning for three-dimensional imaging," *IEEE Transactions on Industrial Informatics*, vol. 15, no. 2, pp. 1173–1182, 2018.

[15] M. Victorova, D. Navarro-Alarcon, and Y. P. Zheng, "3D ultrasound imaging of scoliosis with force-sensitive robotic scanning," in *Proceedings of the 2019 Third IEEE International Conference on Robotic Computing (IRC)*, Naples, Italy, pp. 262–265, 2019.

[16] F. Suligoj, C. M. Heunis, J. Sikorski, *et al.*, "Robust – An autonomous robotic ultrasound system for medical imaging," *IEEE Access*, vol. 9, pp. 67456–67465, 2021.

[17] J. Qi, M. Y. Ding, and M. Yuchi, "3D ultrasound data acquisition system based on back end scan mode," in *Proceedings of 2011 International Conference on Intelligent Computation and Bio-Medical Instrumentation*, Wuhan, China, pp. 156–158, 20118.

[18] C. Y. Xu, G. P. Li, Q. H. Huang, *et al.*, "Establishment of a 3D ultrasound imaging system based on pulse-triggered image acquisition," *Journal of Southern Medical University*, vol. 41, no. 5, pp. 767–774, 2021. (in Chinese)

[19] V. S. Chan, F. Mohamed, Y. A. Yusoff, *et al.*, "Using game controller as position tracking sensor for 3D freehand ultrasound imaging," *Medical & Biological Engineering & Computing*, vol. 58, no. 5, pp. 889–902, 2020.

[20] Q. Q. Cai, C. Peng, J. Y. Lu, *et al.*, "Performance enhanced ultrasound probe tracking with a hemispherical marker rigid body," *IEEE Transactions on Ultrasonics, Ferroelectrics, and Frequency Control*, vol. 68, no. 6, pp. 2155–2163, 2021.

[21] A. Lang, P. Mousavi, G. Fichtinger, *et al.*, "Fusion of electromagnetic tracking with speckle-tracked 3d freehand ultrasound using an unscented Kalman filter," in *Proceedings of SPIE 7265, Medical Imaging 2009: Ultrasonic Imaging and Signal Processing*, Lake Buena Vista, Florida, USA, article no.72651A, 2009.

[22] T. R. Nelson and D. H. Pretorius, "Interactive acquisition, analysis, and visualization of sonographic volume data," *International Journal of Imaging Systems and Technology*, vol. 8, no. 1, pp. 26–37, 1997.

[23] D. G. Gobbi and T. M. Peters, "Interactive intra-operative 3D ultrasound reconstruction and visualization," in *Proceedings of the 5th International Conference on Medical Image Computing and Computer-Assisted Intervention*, Tokyo, Japan, pp. 156–163, 2002.

[24] Q. H. Huang, Y. P. Zheng, M. H. Lu, *et al.*, "Development of a portable 3d ultrasound imaging system for musculoskeletal tissues," *Ultrasonics*, vol. 43, no. 3, pp. 153–163, 2005.

[25] S. Sherebrin, A. Fenster, R. N. Rankin, *et al.*, "Freehand three-dimensional ultrasound: implementation and applications," in *Proceedings of SPIE 2708, Medical Imaging 1996: Physics of Medical Imaging*, Newport Beach, CA, USA, pp. 296–303, 1996.

[26] J. W. Trobaugh, D. J. Trobaugh, and W. D. Richard, "Three-dimensional imaging with stereotactic ultrasonography," *Computerized Medical Imaging and Graphics*, vol. 18, no. 5, pp. 315–323, 1994.

[27] R. Rohling, A. Gee, and L. Berman, "A comparison of freehand three-dimensional ultrasound reconstruction techniques," *Medical Image Analysis*, vol. 3, no. 4, pp. 339–359, 1999.

[28] Q. H. Huang, Y. P. Huang, W. Hu, *et al.*, "Bezier interpolation for 3-D freehand ultrasound," *IEEE Transactions on Human-Machine Systems*, vol. 45, no. 3, pp. 385–392, 2015.

[29] H. B. Chen, R. Zheng, E. Lou, *et al.*, "Compact and wireless freehand 3D ultrasound real-time spine imaging system: A pilot study," in *Proceedings of the 2020 42nd Annual International Conference of the IEEE Engineering in Medicine & Biology Society (EMBC)*, Montreal, Canada, pp. 2105–2108, 2020.

[30] W. W. Jiang, X. T. Chen, and C. H. Yu, "A real-time freehand 3D ultrasound imaging method for scoliosis assessment," *Journal of Applied Clinical Medical Physics*, vol. 23, no. 8, article no. e13709, 2022.

[31] S. W. Xing, D. W. Cool, L. Gardi, *et al.*, "A 2D/3D US/CT-guided system for percutaneous focal liver thermal ablation," in *Proceedings of SPIE 12034, Medical Imaging 2022: Image-Guided Procedures, Robotic Interventions, and Modeling*, San Diego, CA, USA, article no.1203413, 2022.

[32] T. X. Wen, C. Wang, Y. Zhang, *et al.*, "A novel ultrasound probe spatial calibration method using a combined phantom and stylus," *Ultrasound in Medicine & Biology*, vol. 46, no. 8, pp. 2079–2089, 2020.

[33] Y. F. Lv, Y. Ning, Y. Shen, *et al.*, "A real-time interactive 3D ultrasound imaging system," in *Proceedings of 2022 WRC Symposium on Advanced Robotics and Automation (WRC SARA)*, Beijing, China, pp. 113–119, 2022.

[34] F. Rousseau, P. Hellier, and C. Barillot, "A novel temporal calibration method for 3-D ultrasound," *IEEE Transactions on Medical Imaging*, vol. 25, no. 8, pp. 1108–1112, 2006.

[35] P. W. Hsu, G. M. Treece, R. W. Prager, *et al.*, "Comparison of freehand 3-D ultrasound calibration techniques using a stylus," *Ultrasound in Medicine & Biology*, vol. 34, no. 10, pp. 1610–1621, 2008.

[36] K. S. Arun, T. S. Huang, and S. D. Blostein, "Least-squares fitting of two 3-D point sets," *IEEE Transactions on Pattern Analysis and Machine Intelligence*, vol. PAMI-9, no. 5, pp. 698–700, 1987.

[37] Q. H. Huang and Z. Z. Zeng, "A review on real-time 3D ultrasound imaging technology," *BioMed Research International*, vol. 2017, article no. 6027029, 2017.

[38] T. R. Nelson and D. H. Pretorius, "Three-dimensional ultrasound imaging," *Ultrasound in Medicine & Biology*, vol. 24, no. 9, pp. 1243–1270, 1998.

[39] S. Virga, O. Zettinig, M. Esposito, *et al.*, "Automatic force-

compliant robotic ultrasound screening of abdominal aortic aneurysms," in *Proceedings of 2016 IEEE/RSJ International Conference on Intelligent Robots and Systems (IROS)*, Daejeon, Korea, pp. 508–513, 2016.

Yifei LYU received the B.E. degree in the School of Mechanical Engineering and Automation, Beihang University, Beijing, China, in 2022. In 2022, he joined Department of Mechanical Engineering, Tsinghua University, Beijing, China, as an M.E. candidate. His current research interests include medical robot and robot for rehabilitation.
(Email: 15830673175@163.com)

Yu SHEN received the B.S., M.S., and Ph.D. degrees from Northwest University, Xi'an, in 2006, 2009, and 2018, respectively. She is currently a Postdoctoral Researcher with the School of Mechanical Engineering and Automation, Beihang University, Beijing, China. Her research interests include medical image computing and biosensors

Mingbo ZHANG received the M.D. degree in Peking University Health Science Center, Beijing, China, in 2010. In 2010, she joined the General Hospital of Chinese PLA, as a radiologist and researcher. In 2017, she was promoted to Associated Chief Physician and Associate Professor. Her current research interest includes application research of ultrasound guided interventional operation, ultrasound image navigation and ultrasound diagnosis and minimally invasive treatment of thyroid tumors.

Junchen WANG received the B.S. and Ph.D. degrees in mechanical engineering from Beihang University, Beijing, China, in 2006 and 2012, respectively. He was a Postdoctoral Fellow with the University of Tokyo, Tokyo, Japan, from 2012 to 2016. He is currently an Associate Professor at Beihang University. He has authored more than 100 peer-reviewed articles published in international journals and conference proceedings. His research interests include medical robotics, surgical navigation, and medical image computing.
(Email: wangjunchen@buaa.edu.cn)